Volume 10 | Number 6 | June 2017 | Pages 1287–1542

Energy & Environmental Science

rsc.li/ees

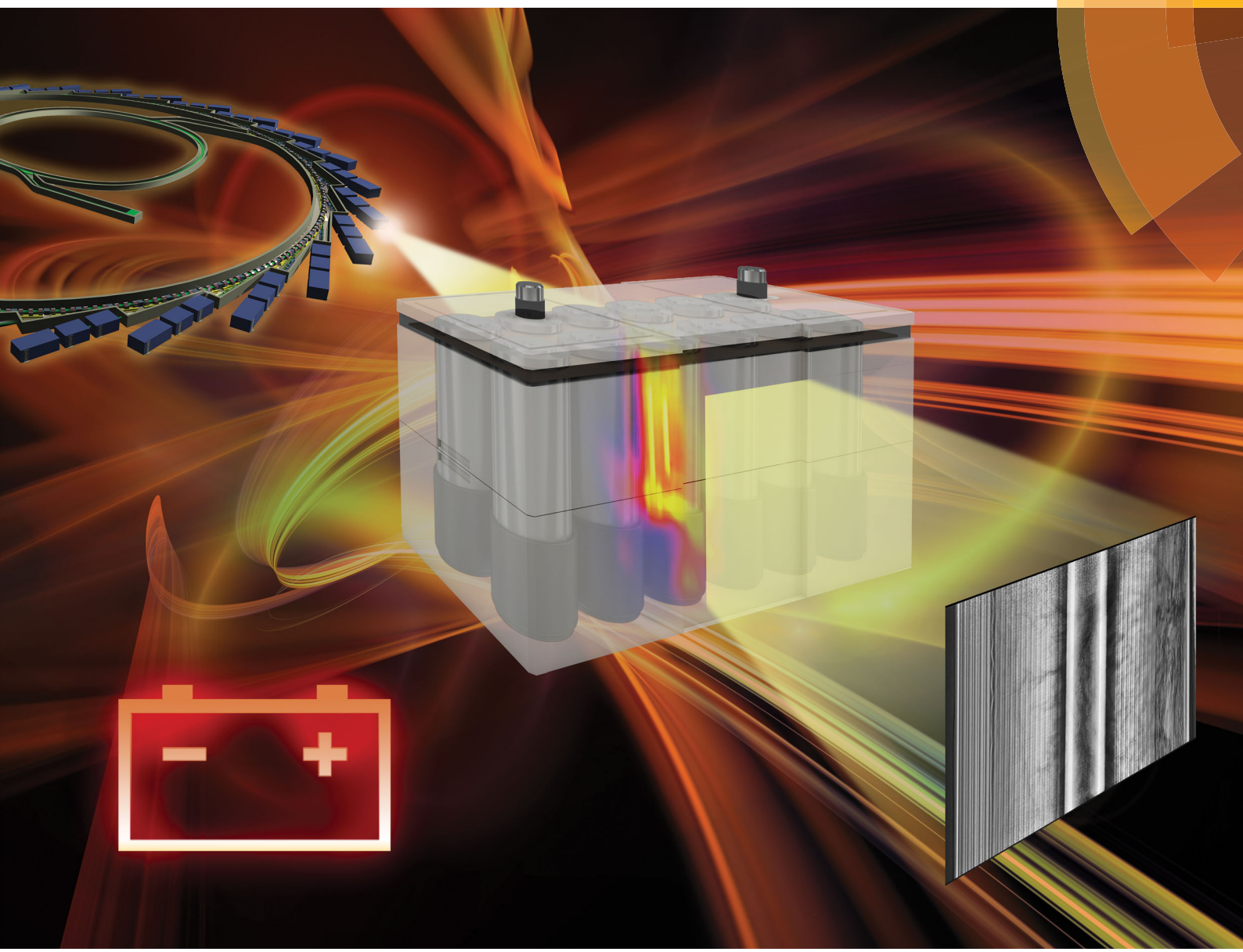

ISSN 1754-5706

ROYAL SOCIETY OF CHEMISTRY

PAPER
Paul R. Shearing *et al.*
Characterising thermal runaway within lithium-ion cells by inducing and monitoring internal short circuits

Energy & Environmental Science

PAPER

View Article Online
View Journal | View Issue

Cite this: *Energy Environ. Sci.*, 2017, **10**, 1377

Characterising thermal runaway within lithium-ion cells by inducing and monitoring internal short circuits†

Donal P. Finegan,[a] Eric Darcy,[b] Matthew Keyser,[c] Bernhard Tjaden,[a] Thomas M. M. Heenan,[a] Rhodri Jervis,[a] Josh J. Bailey,[a] Romeo Malik,[d] Nghia T. Vo,[e] Oxana V. Magdysyuk,[e] Robert Atwood,[e] Michael Drakopoulos,[e] Marco DiMichiel,[f] Alexander Rack,[f] Gareth Hinds,[g] Dan J. L. Brett[a] and Paul R. Shearing *[a]

Received 9th February 2017,
Accepted 17th March 2017

DOI: 10.1039/c7ee00385d

rsc.li/ees

Lithium-ion batteries are being used in increasingly demanding applications where safety and reliability are of utmost importance. Thermal runaway presents the greatest safety hazard, and needs to be fully understood in order to progress towards safer cell and battery designs. Here, we demonstrate the application of an internal short circuiting device for controlled, on-demand, initiation of thermal runaway. Through its use, the location and timing of thermal runaway initiation is pre-determined, allowing analysis of the nucleation and propagation of failure within 18 650 cells through the use of high-speed X-ray imaging at 2000 frames per second. The cause of unfavourable occurrences such as sidewall rupture, cell bursting, and cell-to-cell propagation within modules is elucidated, and steps towards improved safety of 18 650 cells and batteries are discussed.

Broader context

From portable electronics to grid-scale storage, high energy density Li-ion batteries are ubiquitous in today's society. Such cells can and do fail, sometimes catastrophically, releasing large amounts of energy. To facilitate safer and more reliable cell designs, the importance of understanding failure mechanisms of Li-ion cells is widely recognised. Here, we demonstrate the application of a novel device that is capable of generating an internal short circuit within commercial cell designs, on-demand, and at a pre-determined location. This enables us to test more effectively the ability of safety devices of cells and modules to withstand 'worst-case' failure scenarios. By combining the use of this device with high-speed X-ray imaging at 2000 frames per second, we characterise for the first time the initiation and propagation of thermal runaway from a known location within a Li-ion cell. The insights achieved in this study are expected to guide the design and development of safer and more reliable Li-ion cells.

1. Introduction

The demand for Li-ion batteries is expected to rapidly increase over the coming years,[1] but concerns over their safety and reliability hinders their uptake, in particular for applications that require exceptionally low risk, such as communications[2] and space exploration.[3,4] Although catastrophic failure of lithium-ion cells is extremely rare, recent high-profile events have demonstrated the high socioeconomic risks associated with battery failure; for example, the recall of an entire product line of smartphones[5] and the grounding of an aircraft fleet[6] following the catastrophic failure of Li-ion batteries. Improving the safety and reliability of Li-ion batteries is essential for 'mission critical' applications.

Internal short circuits (ISCs) within Li-ion cells can lead to thermal runaway by providing enough heat to trigger a series of exothermic reactions,[7–12] and are consequently of great concern to battery manufacturers, particularly since they can stem from latent defects from manufacturing, which are difficult to detect.[13] The maximum temperature reached during a short circuit, and therefore the likelihood of a short circuit leading to

[a] *Electrochemical Innovation Lab, Department of Chemical Engineering, University College London, Torrington Place, London, WC1E 7JE, UK. E-mail: p.shearing@ucl.ac.uk*
[b] *NASA-Johnson Space Center, Houston, TX, 77058, USA*
[c] *National Renewable Energy Laboratory, 15013 Denver West Parkway, Golden, CO 80401, USA*
[d] *Warwick Manufacturing Group, University of Warwick, Coventry CV4 7AL, UK*
[e] *Diamond Light Source, The Harwell Science and Innovation Campus, Didcot, Oxfordshire OX110DE, UK*
[f] *ESRF The European Synchrotron, 71 Rue des Martyrs, 38000 Grenoble, France*
[g] *National Physical Laboratory, Hampton Road, Teddington, Middlesex, TW11 0LW, UK*

† Electronic supplementary information (ESI) available. See DOI: 10.1039/c7ee00385d

thermal runaway, depends on the electrical and thermal conduction properties of the materials that make unintentional contact.[14,15] For example, contact between the positive Al current collector and the negative Cu current collector would provide the most rapid discharge and heat generation, but the heat would dissipate relatively quickly due to the high thermal conductivity of the materials. A short circuit between the Al current collector and the carbon negative electrode would also result in rapid discharge and heat generation due to the two materials having high electrical conductivities; however, the relatively low thermal conductivity of the porous carbon electrode would lead to locally higher temperatures, and therefore an increased risk of thermal runaway initiating.

The risks associated with the occurrence of thermal runaway depend on the design of the cell or module; pouch cells that are not contained within a rigid shell tend to swell and catch fire, whereas 18 650 cylindrical cells, which consist of a spiral-wound electrode assembly contained within a rigid steel container, can fail *via* violent rupture or explosion due to the container acting as a pressure vessel.[16] Numerous safety devices are included in today's 18 650 cells to help avoid or mitigate catastrophic failure, such as pressure relief vents, current interrupt devices (CIDs) and positive temperature coefficient (PTC) current-limiting switches.[17] Similarly, external safety devices such as battery management systems (BMSs) and temperature control in modules and systems help avoid unfavourable conditions. Whilst these devices can help maintain safe operating conditions, they cannot prevent the occurrence of ISCs in defective cells, which remain a risk in battery-powered systems where cell-to-cell propagation of thermal runaway can occur. An improved understanding of the thermal and structural dynamics associated with ISCs would help manufacturers develop safer battery designs and modules to minimise the risk associated with such failures. However, internal short circuiting and the process of thermal runaway, as well as the influence of mechanical designs and safety features on the failure mechanism, are not yet well-understood.

Over the past decade, X-ray radiography and computed tomography (CT) have emerged as effective, non-destructive tools for characterising battery degradation and failure.[18,19] In particular, the rapidly advancing capabilities of X-ray CT systems[20,21] present scope for capturing failure events and degradation mechanisms across multiple length scales[9] and over very short time periods.[16,22] The high-speed imaging capability of synchrotrons allows temporal studies of evolving material microstructures or device architectures in 3D, which has recently been used to reveal degradation mechanisms from the electrode particle[23] to the full cell level.[16,24] However, characterising the process of thermal runaway is extremely challenging, primarily due to the rapid change in material architecture and the unpredictability of the location at which thermal runaway initiates.[16] This needs to be known in order to set the field-of-view of the X-ray and orientation of the cell such that the initiation and propagation of thermal runaway can be successfully imaged.

Numerous attempts to replicate an ISC have previously been made. Maleki *et al.*[25] induced an ISC through nail penetration, indentation and pinching of cells. Orendorff *et al.*[26] described an ISC device that involves placing a low melting point metal between the positive electrode and the separator, which when melted would penetrate through the separator and cause a short circuit; a technique that has not yet been proved to be reliable. The 2015 International Electrotechnical Commission (IEC) testing standard[27] describes a technique for forced internal short circuiting (FISC) by incorporating a metallic particle into the electrode assembly and subjecting it to compression; however, this method involves dismantling the cell and does not provide information about actual cell behaviour during an internal short, which is determined by the cell design and integrated safety devices. Hence, there is a need for a reliable test method that replicates the behaviour of an unmodified commercial cell design undergoing an ISC to better understand thermal runaway propagation and evaluate the efficacy of safety devices.[28]

Here, the characterisation of an ISC device developed at NASA and NREL by Keyser and Darcy[29] is presented. The ISC device, which is implanted inside 18 650 test cells during assembly, can achieve an on-demand failure at a pre-determined location within the cell, which is representative of a latent defect, 'in-field' failure. By being able to control the location at which thermal runaway initiates, 'worst-case' failure scenarios, such as cell bursting or sidewall rupture can be induced, allowing insight into cell design vulnerabilities. The provision of ISCs at a pre-determined location allows replication of initiation and analysis of thermal runaway propagation through the use of X-ray imaging.[25] Until now, due to the small field-of-view associated with high-speed imaging, capturing the rapid events surrounding initiation and propagation of thermal runaway was left to chance. The initiation and propagation of thermal runaway resulting from an ISC is captured, using high-speed (*ca.* 2000 frames per second) X-ray imaging at The European Synchrotron (ESRF)[22,30] and Diamond Light Source (DLS) synchrotron. This has provided unprecedented insights into the failure mechanisms and the influence of cell design[16] on the safety of 18 650 cells. Furthermore, 18 650 cells with an ISC device, located in such a way as to induce sidewall rupture, are placed in 2 × 2 modules of 18 650 cells in order to study cell-to-cell propagation and the safety concerns that such a mode of thermal runaway may cause for multi-cell modules.

2. Experimental

2.1. Internal short circuiting device

The ISC device[29] was designed to generate an electrical short between two electrically conducting layers. In this work, the ISC device connects the negative electrode active material to the positive electrode current collector, bypassing the less electrically conductive positive electrode active material (Fig. 1). This has been suggested to be the type of short that is most likely to result in thermal runaway, as shown by Santhanagopalan *et al.*[15] and confirmed by Shoesmith,[31] since the negative carbon electrode maintains high electrical conductivity (to cater for a rapid short circuit and heat generation), but a lower thermal conductivity than the Cu current collector (resulting in a lower rate of heat dissipation).

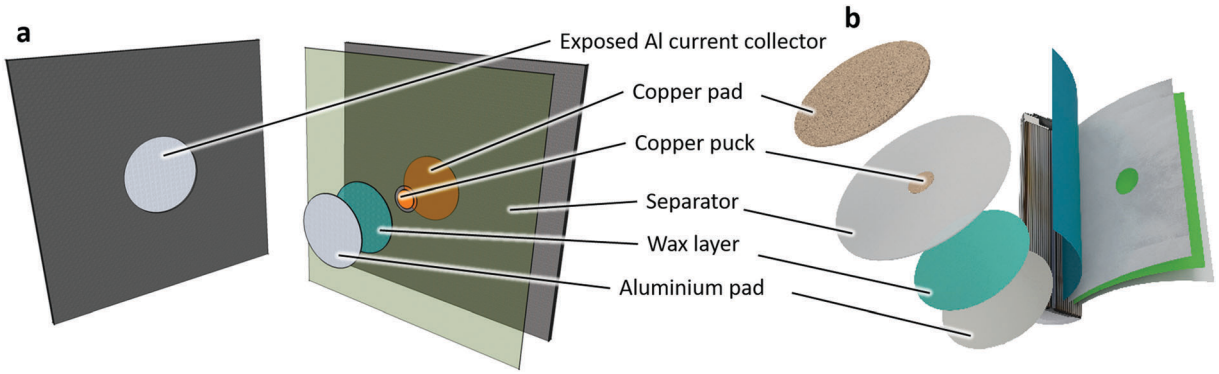

Fig. 1 (a) Exploded view of the individual components of the ISC device, where the positive electrode material is etched away for seating the Al pad. (b) 3D illustration showing where the components of the ISC device are inserted into the spiral-wound electrode assembly of an 18 650 cell.

The ISC device used in this work consisted of four layers (Fig. 1): a 76 μm thick Al pad with a diameter of 11.11 mm, a thin (10–20 μm) layer of electrically conductive wax (consisting of a mixture of microcrystalline and paraffin wax) that melts at 57 °C, a 25 μm thick Cu puck with a diameter of 3.18 mm, and a 25 μm thick Cu pad with a diameter of 11.11 mm. The crucial component of the ISC device was the thin (10–20 μm) and uniform wax layer on the side of the Al pad adjacent to the Cu puck whose deposition was achieved through a spin coating process. The device also included a separator layer that matched the separator of the implanted cell, making up the gap between the Cu and Al pads outside the area of the Cu puck. Activation of the ISC device generally occurs when the wax melts (at 57 °C) and is expected to be wicked away by the surrounding separator, providing an electronically conducting path between the negative carbon electrode and the positive Al current collector.

Once the ISC device had been assembled, implantation began by unwinding dry spiral-wound electrode assemblies to uncover the desired short location. In this study, the positive electrode coating was removed to expose the Al current collector (Fig. 1a) by unravelling the electrode, placing a nylon template with a 14.29 mm diameter hole on the surface of the electrode layer, and using an acetone-soaked cloth to remove the electrode active material. In a dry electrode assembly, the Al side of the assembled ISC device was then seated into the hole in contact with the Al current collector (Fig. 1a). A corresponding, oversized and aligned hole was made in the cell separator to allow the Cu pad side of the ISC device to contact the negative electrode active material. The separator of the device and of the cell, were adhered together with a small amount of glue to secure the device in place during rewinding of the electrode assembly. Once the electrode assembly had been rewound, an isolation resistance test was performed before returning to the cell assembly process.

To further increase the likelihood of a thermal runaway response and maximise its effects, the cells were made with a single-layer polypropylene separator (with no shutdown feature). Previous cells made with a tri-layer shutdown separator were found to effectively inhibit ionic flow and reduce the chance of catastrophic thermal runaway response to collector–collector shorts.[32] In these implantations, the wax-coated aluminium pad was oriented towards the centre of the electrode assembly.

Two different batches of 18 650 test cells were implanted and are shown in Fig. 2; one with the ISC device placed at mid-longitudinal height (Fig. 2a) and six winds (from a total of 18) into the spiral-wound electrode assembly (henceforth referred to as 'ISC 1'), and the second with the ISC device at mid-longitudinal height and three winds into the electrode assembly (henceforth referred to as 'ISC 2'). Two radial depths were tested to examine the influence of the location of failure initiation on the failure mechanism of the cells. The ISC 1 cells had a capacity of 2.4 A h with an internal cylindrical mandrel (Fig. 2b), and the ISC 2 cells had a capacity of 3.5 A h with no internal mandrel (Fig. 2c). To date, this batch of over 36 cells has yielded 100% success at inducing thermal runaway response with 16 cells activated at 100% state of charge (SOC). In order to safely ship these test cells, it was verified that activation at 0% SOC results in a hard short but only a small temperature rise.

High-resolution synchrotron X-ray CT (imaging details are provided in Section 2.3) was used for quality inspection (Fig. 2b–e). Fig. 2d and e show that there is a significant distance between the circumference of the Al pad and the positive electrode material; in the immediate vicinity of the circumference of the pad, the separator layer is seen to make contact directly with the Al current collector. Furthermore, a pinch point is observed between the Cu and Al pad where the separator may be under additional compressive strain; this could weaken and close the pores of the separator around these regions. This pinch point is expected to affect the propagation of thermal runaway, and is discussed in the Results section.

2.2. Setup, heating and temperature measurement

A modified nail penetration tester (MSK-800-TE9002, MTI Corporation, USA) with infra-red and X-ray transparent windows was used to secure the cells for imaging and to act as a containment system for the failing cells. Further details and images of the system are provided in the ESI.† The 18 650 cells were held firmly in place by hydraulic clamps to keep the region of interest in the field-of-view for the entire duration of the battery failure.

The test cells were heated using a custom, 12 mm tall, circumferential NiCr wire heater with a length equivalent to a 5 Ω resistance located at the bottom side wall of the cell (Fig. 2a). The high resistance coil was connected to a DC power supply that was operated at 10 V and 1.83 A, providing a heating power of 18.3 W (of which *ca.* 16.7 W was applied to the cell and the rest was

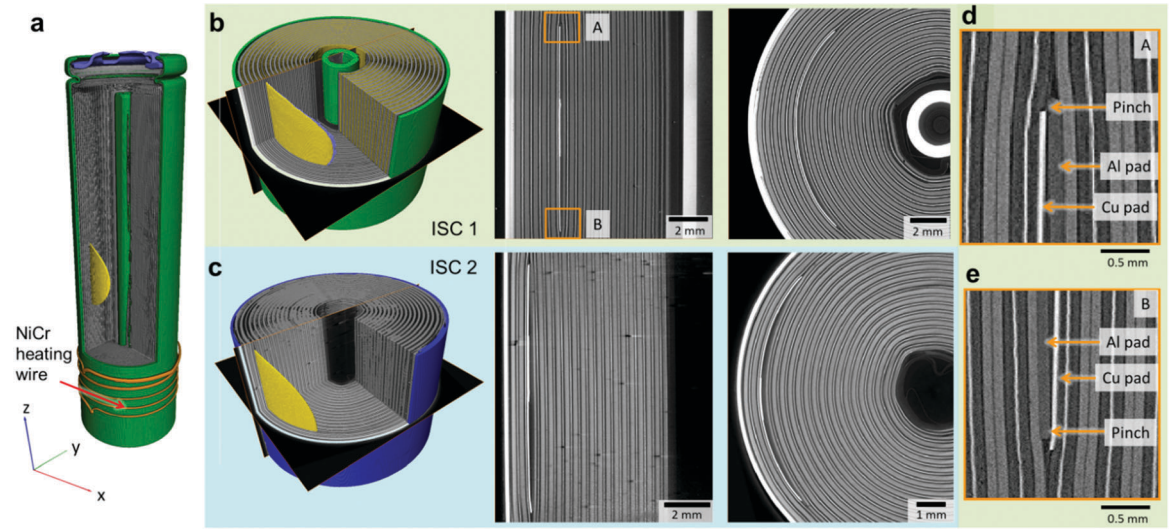

Fig. 2 (a) 3D reconstruction of a full 18 650 test cell showing the longitudinal location of the ISC device (yellow) and the NiCr heating wire (orange). (b) 3D reconstructions and associated *YZ* and *XY* slices with labelled regions of interest (A and B) showing placement of the ISC device six layers into the electrode assembly (ISC 1), and (c) three layers into the electrode assembly (ISC 2). (d) Magnified view of the top end of the ISC pads from a *YZ* slice of the ISC 1 cell labelled A, and (e) bottom end of the ISC pads labelled B. A pinch point between the Cu and Al pad is highlighted by arrows.

dissipated in the cables and connections). The power was applied immediately for the ISC 1 cells and gradually ramped up to the required power for the ISC 2 cells. After prolonged heating at a power of 18.3 W, the cells in which the ISC device had not activated at the expected temperature of *ca.* 60 °C, were exposed to gradually increasing power until activation occurred. This delayed response is suspected to occur as a result of insufficient winding tension in the electrode assembly for the Cu puck to press through the wax.

The temperature of the surface of the cells was measured using a thermal camera (FLIR SC5000MB, FLIR Systems France, Croissy-Beaubourg, France), which was separated from the battery failure by a 2 mm thick infra-red transparent sapphire window (set-up shown in ESI†). The 18 650 cells were painted with a uniform layer of heat-resistant black paint with a calibrated emissivity[33] of 0.96 over the range of 40–180 °C. The calibrated temperature range of the thermal camera that was used in this experiment was 15–250 °C. The InSb detector of the thermal camera allowed detection of infra-red wavelengths between 2.5 μm and 5.1 μm, the noise equivalent temperature difference of the camera was <20 mK for the calibrated range, and the measurement accuracy was ± 1 °C or 1% of the measured temperature in degrees Celsius. Thermal images were recorded at a rate of 25 Hz.

Due to prolonged exposure to high energy X-rays, the detector readings from the thermal camera became less reliable, hence for the ISC 2 cells temperature readings were gathered from a fast response K-type thermocouple with a diameter of 0.5 mm (product 406-534, TC Direct, Uxbridge, UK) that was applied to the surface of the cells using aluminium tape.

2.3. Tomography and high-speed X-ray imaging

Lab-based X-ray CT. A tomogram of a full 18 650 cell with an integrated ISC device was captured using a lab-based X-ray CT system (Zeiss Xradia 520 Versa, Carl Zeiss Microscopy, Pleasanton, CA, USA). A 0.4× optical magnification was used, and the sample-to-source and source-to-detector distances were 32.2 mm and 79.4 mm, respectively, giving a pixel size of 19.82 μm. With an exposure time of 2 s and a source voltage of 160 kV, 2001 images of 1024 × 1024 pixels were used to reconstruct the individual tomograms. Five tomograms along the length of the 18 650 cell were reconstructed using Zeiss XMReconstructor software which uses a filtered back projection (FBP) algorithm, and were stitched together (vertically) using the software's automatic stitching option.

Synchrotron X-ray CT. A higher resolution tomogram of the section of the ISC 1 cell with the integrated ISC device was achieved at beamline ID19 at The European Synchrotron (ESRF), and a similar tomogram of the ISC 2 cell was captured at beamline I12 at Diamond Light Source (DLS) synchrotron.[34]

At the ESRF, the ISC 1 cell was imaged using a polychromatic beam with a field-of-view (FOV) of 9.65 mm × 15.20 mm (horizontal × vertical) which consisted of 1302 × 2048 pixels with a pixel resolution of 7.42 μm. This FOV corresponded to half the cell in the horizontal direction. The rotation axis of the sample was located at the edge of the FOV such that by rotating the sample 360° it was possible to image and reconstruct the entire sample.[35] A total of 3600 images with an exposure time of 0.2 s, taken at angular increments of 0.1°, were used for the reconstruction. A high-speed PCO.Dimax (PCO AG, Germany) detector and a LuAG:Ce ($Lu_3Al_5O_{12}$:Ce) scintillator were used for capturing tomograms at the ESRF. The tomograms were reconstructed using the standard FBP.

At DLS, the ISC 2 cell was imaged using a monochromatic 74 keV beam with a FOV of 20.22 mm × 17.06 mm which consisted of 2560 × 2160 pixels with a pixel resolution of 7.9 μm. A total of 2400 images, each with an exposure of 2.5 ms, were taken for a 180° rotation. A PCO.Edge detector (PCO AG, Germany) and a LuAG:Ce scintillator were used for acquisition of the tomograms. At DLS, the tomograms were reconstructed using

the DAWN reconstruction software package[36] that utilises FBP and ring removal.[37]

High-speed radiography. For the ISC 1 cells, a polychromatic beam was used for high-speed radiography in the ID19 beamline[22] at the ESRF, with a high-speed PCO.Dimax (PCO AG, Germany) detector and GGG:Eu ($Gd_3Ga_5O_{12}$:Eu) scintillator. The FOV was 22.89 mm × 14.67 mm (horizontal × vertical) which consisted of 2016 × 1292 pixels with a pixel size of 11.35 μm. Images were captured at a rate of 2000 frames per second (fps) (with an exposure time of 461 μs) for samples 1 to 5, and 1000 fps (with an exposure time of 957 μs) for sample 6. The best radiography view to observe the initiation and propagation of failure from the ISC device was from the side where the Cu puck was placed, such that it was parallel with the beam. This orientation gave a clear view of how the failure propagated in the cell.

For the ISC 2 cells, a monochromatic 74 keV beam was used for high-speed radiography at beamline I12 at DLS, along with a Vision Research Phantom Miro 310 high-speed detector (Vision Research, NJ, USA) and LuAG:Ce scintillator. The ISC 2 cells were imaged with a FOV of 22.91 mm × 14.32 mm consisting of 1280 × 800 pixels (horizontal × vertical) with a pixel size of 17.9 μm, at 2000 fps using an exposure time of 490 μs.

3. Results and discussion

3.1. Activation of ISC device

When activated, the wax layer (Fig. 1) separating the positive Al current collector and the negative carbon electrode, melts and is wicked away with the aid of the winding tension of the electrode assembly causing the type of short circuit that is most likely to lead to thermal runaway.[14,15] All cells were tested at 100% SOC; the fully lithiated negative electrode is most susceptible to thermal runaway since at high temperatures the lithium from the graphite reacts with the electrolyte, releasing heat.[38] Hence, here we aim to present the worst-case failure type of a Li-ion cell within a recommended operating voltage range.

The wax layer is expected to melt, and the short circuit to occur, when the battery reaches *ca.* 57 °C. For the ISC 1 cells, four samples out of six exhibited this anticipated behaviour (Fig. 3a), whereas two samples showed a delayed response and required further heating to *ca.* 100 °C before thermal runaway occurred (sample 1 and sample 6). It is suspected that for these samples the winding tension was insufficient for the Cu puck to push the wax out until higher temperatures (and lower viscosity) were achieved. Similarly, the three ISC 2 cells showed a delayed response and thermal runaway initiated at *ca.* 100 °C (Fig. 3b). The difference in the shape of the temperature profile in Fig. 3a and b, stems from the different heating strategy used during imaging of the ISC 1 cells at the ESRF, where full power was applied immediately, and the ISC 2 cells at DLS where the heating power was gradually ramped up. The thermal images in Fig. 3 were taken 1 s before thermal runaway occurred and show the location of the heating pad as well as the temperature profile across the surface of the cell during heating.

When thermal runaway occurred, the surface of the cells exceeded the maximum calibrated temperature of the thermal camera, which is observed as a plateau in temperature at just under 250 °C in Fig. 3a. The surface of each of the cells exceeded 250 °C in less than 2 s when thermal runaway occurred, similar to the results from the model of the short circuit between Al current collector and graphite electrode developed by Santhanagopalan *et al.*[15]

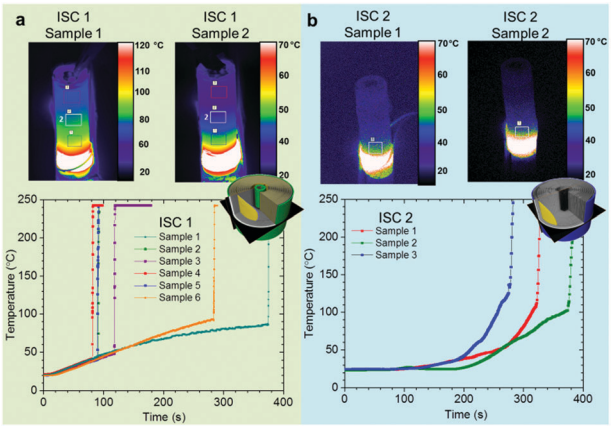

Fig. 3 (a) Top: Thermal images taken 1 s before thermal runaway; a delayed activation occurred for samples 1 and 6. Bottom: Temperature plots showing the mean temperature from the surface area of the cell within region 2 (middle square) in the thermal images. (b) Top: Thermal images taken 1 s before thermal runaway. Bottom: Temperature plots for the ISC 2 cells taken from a thermocouple located mid-way up the cell. Due to prolonged exposure to high-energy X-rays, the thermal images of cell 2 are provided for qualitative purposes only.

3.2. Short circuit and initiation of thermal runaway

Until now, capturing the initiation and subsequent propagation of thermal runaway has proved extremely challenging,[16] requiring high-speed and high-resolution radiography at the exact longitudinal location and azimuthal orientation to get a clear side-on view of the occurrence. The advantage of the ISC device is that it provides a pre-determined location of thermal runaway initiation.

Time-stamped high-speed X-ray radiography videos are provided as Movies S1–S6 (ESI†) for samples 1–6 of the ISC 1 cells, respectively, and Movies S7–S9 (ESI†) for samples 1–3 of ISC 2 cells, respectively. Consistent failure mechanisms were identified during each thermal runaway process. Supplementary movies (ESI†) that best capture certain failure mechanisms will be referred to throughout the text.

As shown in Fig. 4, thermal runaway propagated from the outer circumference of the Cu and Al pads (Fig. 2d and e), rather than the inner Cu puck, for each of the samples. However, in samples 1 and 5 of the ISC 1 cells, there appeared to be slight movement around the puck region approximately 0.005 s before propagation of thermal runaway began at the circumference of the pad (1.3950 s in Movie S1 and 1.3385 s in Movie S5, ESI†). This indicates that thermal runaway activated at the puck where local gas generation caused movement of the layers. Short circuiting then occurred at the perimeter of the pad (Fig. 4c), from where the degradation of the active materials was seen to occur most rapidly. Five out of the six ISC 1 cells, and two out of three of the ISC 2 cells, clearly showed propagation of thermal runaway from the top or bottom of the circumference of the pads.

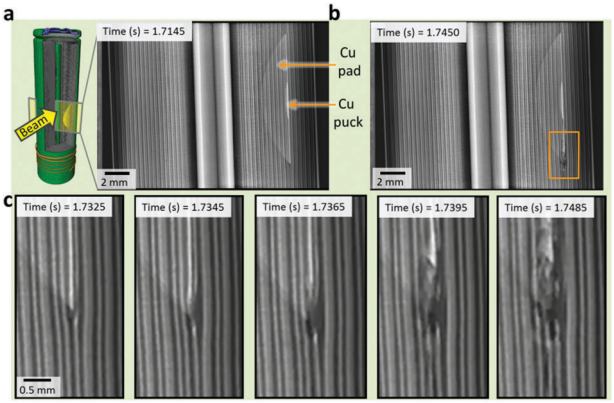

Fig. 4 (a) 3D illustration showing the field-of-view of the beam, and corresponding radiograph showing the location of the ISC device within sample 6. (b) Radiograph showing the location from which propagation of thermal runaway occurred (region of interest within orange box). (c) Magnified section of the region of interest from the radiographs showing the early stages of thermal runaway propagation.

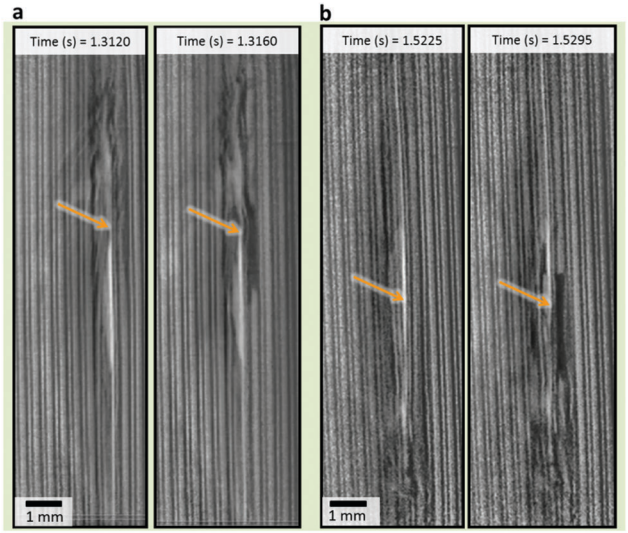

Fig. 5 Radiographs showing before and after snapping of the separator for (a) sample 3 and (b) sample 5 of the ISC 1 cells, extracted from Movies S3 and S5, respectively (ESI†).

It is suspected that due to the separator being pinched between the Al and Cu around the perimeter of the pads (Fig. 2d and e), the local temperature rise resulting from the short circuit at the Cu puck caused shrinkage and strain on the separator. The separator for the ISC 1 cells consists of a polypropylene (PP) monolayer manufactured by dry processing,[39] which involves uniaxial stretching of polymer lamellae resulting in the formation of 'slit-like' pores;[40] this causes inherent differences in the tensile strength in the machine direction and transverse direction. Having lowest tensile strength in the longitudinal (transverse) direction, the top or bottom of the pinched separator circumference are the most likely locations for tearing of the separator, and therefore shorting to occur (Fig. 4). At the pinch point, propagation stemmed from a short between the Al and Cu current collectors, resulting in rapid discharge of the cell and high rate of local Ohmic heat generation. The Cu and Al current collectors were seen to melt within 0.003 s after the short initiated (Fig. 4c) indicating that local temperatures exceeded the melting point of Cu (>1085 °C).

3.3. Propagation of thermal runaway

Gas pockets formed at either side of the ISC device within 0.05 s following initiation, causing delamination in the longitudinal and azimuthal directions. It is likely that the heat produced from the short circuit caused the electrolyte to vaporise and react with the electrodes. The highly exothermic reactions between the positive electrode material and the electrolyte may have contributed to the rapid propagation in the azimuthal and longitudinal directions through particle-to-particle propagation. This surface reaction process would generate gaseous products between the electrode particles, increasing the porosity of the electrode, delaminating the electrode from the current collector, and ultimately helping to fluidize the microstructure as gaseous products are displaced due to local pressure differences.[9]

The greyscale (and X-ray attenuation) of the positive electrode material in the radiographs reduced rapidly in the longitudinal direction in steps along the radial axis; this is clearly seen in each of the Movies S1–S9 (ESI†). The reduced greyscale was most likely caused by an increase in the electrode porosity, and this was soon followed by fluidization and ejection of the electrode material. The propagation of thermal runaway occurred significantly faster in the longitudinal and azimuthal directions (estimated from samples 1 and 4 of the ISC 1 cells to be between 200–400 mm s^{-1}) than in the radial direction (estimated from all ISC 1 cells to be *ca.* 6–8 mm s^{-1}).

Within 0.2 s after initiation, the separator next to the ISC device snapped causing a jolt in the spiral-wound architecture and aggravating the propagation of thermal runaway (Fig. 5). The pores of the PP separator started to close and the membrane began to shrink at temperatures above 90 °C, causing strain, particularly in the transverse direction.[41] Subsequently, the separator started to melt at 165 °C. Here, snapping of the separator is likely to have been caused by a combination of temperature-induced strain and softening at elevated temperatures. Following the first occurrence of the separator snapping, several occurrences that resemble the initial jolt occurred, but were less severe. This aggravation of thermal runaway could be avoided by using a more thermally stable ceramic or glass-based separator that does not incur shrinkage and strain at the aforementioned temperatures.

In a step-wise manner, thermal runaway propagated radially at approximately equal rates in both directions, until the active material experienced significant displacement, at which point the propagation of thermal runaway was interrupted (Fig. 6). From the ISC 1 device, the propagation spread across four layers in each radial direction, as shown in Fig. 6b. Interruption of thermal runaway usually occurred due to large sections of the electrode ejecting or undergoing significant displacement; for example, Fig. 6b and c taken from sample 1 of the ISC 1 cells (Movie S1, ESI†) show the electrode assembly before and after it partially ejected. The rate of propagation significantly decreased

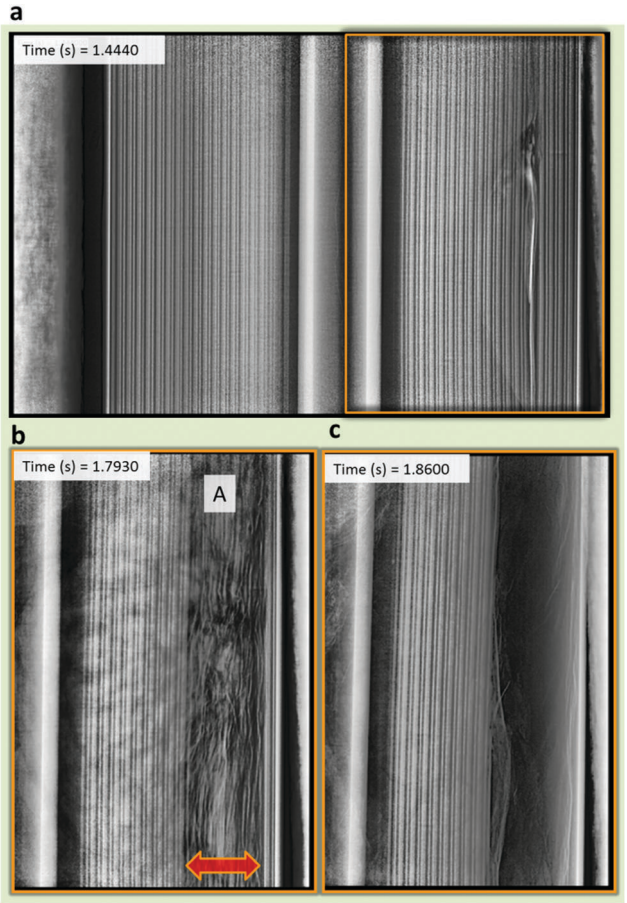

Fig. 6 Radiographs from sample 1 of the ISC 1 cells, demonstrating that from the time of initiation (a), heat transfer and thermal runaway continued radially inwards and outwards (b), until interrupted by detachment or ejection of the active materials (c). These images can be found in Movie S1 (ESI†).

when large sections of the degrading active material (the heat source) were ejected or displaced.

The consistent sequence of events that occurred during the propagation of thermal runaway are presented in Fig. 7a–c. Thermal runaway propagated in all directions from the ISC device, but significantly faster in the azimuthal and longitudinal directions from the point of initiation (Fig. 7a). Propagation in the azimuthal direction is followed by observing the dark shadow (low X-ray attenuation) front moving from the ISC device to the opposite side of the electrode assembly (Fig. 7b). When the dark shadow reaches the opposite side, the electrode material is clearly seen to first degrade six winds in from the casing of the cell (in line with the ISC device). Within 0.5 s, the reaction zone (shown in red in Fig. 7) resembled a hollow cylindrical shape that became noticeably more fluid-like as gases were generated and the degrading materials began to lose their mechanical integrity (Fig. 7b). Kim *et al.*[42] modelled local heat release to simulate a cylindrical cell undergoing an ISC, showing a similar cylindrical reaction zone resulting from fastest propagation in the azimuthal and longitudinal directions. Kim *et al.*[42] also demonstrated that thermal runaway propagates faster radially inwards than outwards; however, it is not evident in this study that this is the case.

Prior to ejection, the broken down active materials surrounding the ISC device shifted towards the base of the cell for each of the ISC 1 samples (Fig. 7c). The electrode material began to eject towards the vent of the cell within *ca.* 0.04 s after the material initially shifted towards the base. It is expected that ignition of the electrolyte and gaseous products from decomposition reactions[43] (ethane, hydrogen, methane and oxygen) occurred at the vent of the cell, where for a brief moment associated with combustion at the vent, the local pressure built up faster than the product gases could escape, causing a short-lived backflow. This shift towards the base of the cell was followed by either partial or complete ejection of the cell contents (Fig. 7d) from the top of the cell.

Two of the six ISC 1 cells burst, which is expected to have been caused by the vent becoming clogged. The electrode material at the core of the cell (where the reaction zone had not yet reached) remained intact and the central mandrel in place – this stable zone is shown as a semi-transparent blue cylinder in Fig. 7b–d. Before the reaction zone reached the inner layers of the spiral-wound cell, the reacting material began to eject and disrupt the propagation of thermal runaway. As the reaction zone became more fluid-like, the intact core (blue region in Fig. 7) detached and moved independently. In both ISC 1 cells that burst (sample 2 and sample 5), the intact core shifted up towards the vent and paused just before the entire electrode assembly ejected, similar to what was observed in a previous study.[16] This suggests that, as a consequence of the reaction zone weakening the spiral-wound architecture, the inner intact core was no longer anchored to the base of the cell and shifted upwards, clogging the vent. The pressure within the cell then exceeded the burst pressure of the crimp causing the sudden ejection.

3.4. Sidewall rupture and location of failure initiation

Sidewall rupture occurred in each of the ISC 2 cells (*e.g.* label A in Fig. 8b), whereas the casing of the ISC 1 cells remained entirely intact (Fig. 8a). The location of thermal runaway initiation within the 18 650 cells is shown to influence the likelihood of sidewall rupture. The occurrence of sidewall rupture was a consequence of high pressures being reached within the cell and weakening of the casing when subjected to high temperatures. At the point of initiation of the short circuit, the discharge of the cell resulted in high temperatures, which are shown in Fig. 4 to be in excess of 1085 °C. In addition to the high temperature, it is expected that a pocket of high pressure also formed in the vicinity of the short circuit, as gases were generated at a high rate and a path of escape had not yet been cleared. The combination of high temperature and high pressure in the vicinity of the point of initiation of thermal runaway presents a high risk for sidewall rupture, particularly as the vicinity of initiation approaches the cell casing. This is examined through the placement of the ISC device at a closer proximity to the cell casing in the ISC 2 cells than in the ISC 1 cells. However, it is important to note that the ISC 2 cell is designed to deliver higher power (>12 W h at 100% SOC) than the ISC 1 cell (<9 W h at 100% SOC)

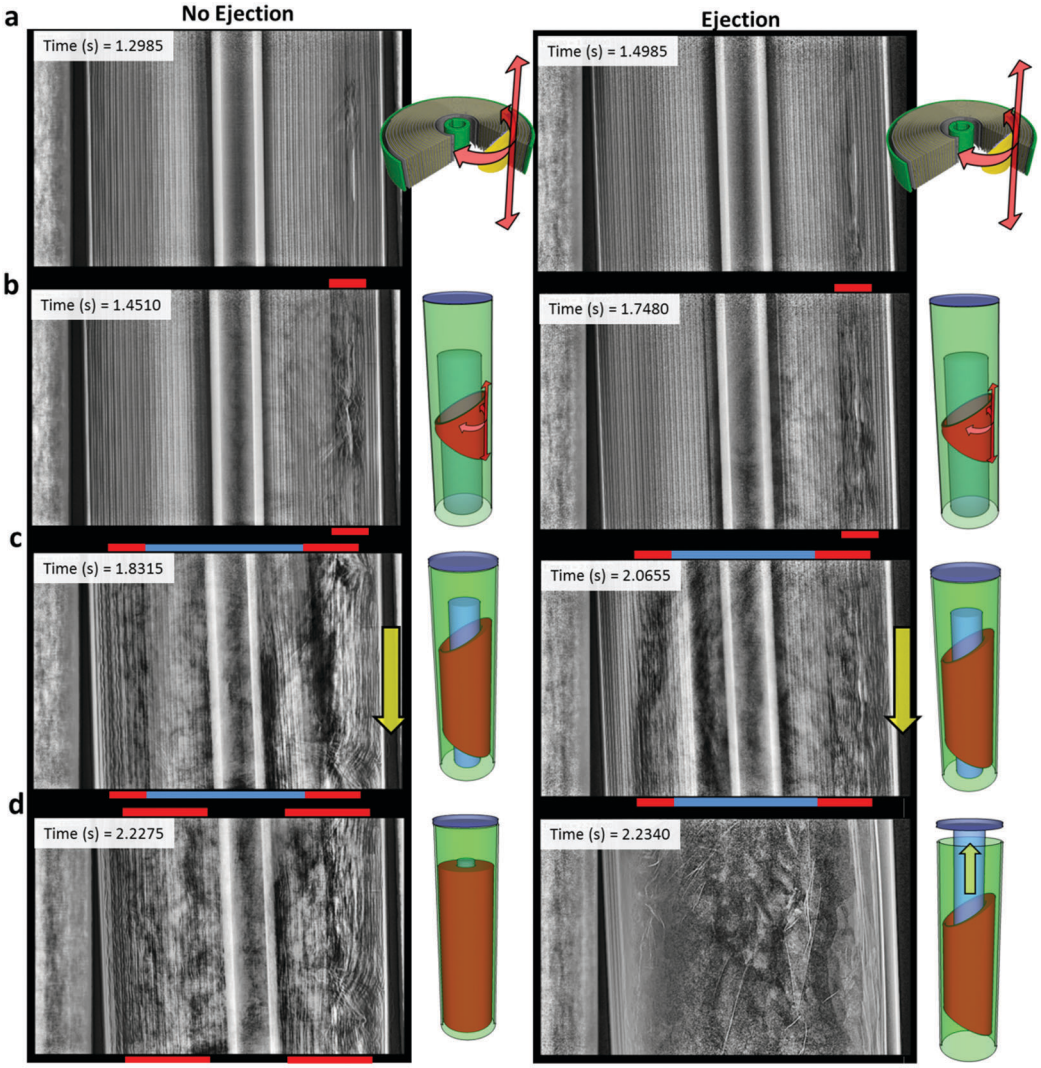

Fig. 7 Radiographs and 3D illustrations showing the propagation of thermal runaway within the ISC 1 cells, resulting in either complete breakdown of active materials within the cell (sample 3 – left column) or ejection of contents *via* the cell bursting (sample 5 – right column). Radiographs and 3D illustrations show that (a) propagation occurred fastest in the longitudinal and azimuthal directions from the ISC device, (b) the azimuthal propagation resulted in a ring-shaped reaction zone (red) around an intact core (semi-transparent blue), (c) as propagation continued in all directions, the intact core (blue) began to move independently, and (d) the reaction either ran to completion within the cell, or the intact core shifted up towards the vent followed by ejection of the electrode assembly. Radiography movies of ISC 1 samples 3 and 5 are provided as Movies S3 and S5, respectively (ESI†).

which may affect the rate at which the cell discharged during short circuiting.

The radiographs from the ISC 1 cells show that approximately 0.5 s elapsed between the initiation of thermal runaway and its propagating front reaching the casing of the cell, whereas the equivalent time in the ISC 2 cells was approximately an order of magnitude faster. This difference in propagation time between the ISC 1 and ISC 2 cells is demonstrated in Fig. 8a and b, where the time between initiation of thermal runaway and the propagation front reaching the casing was 0.414 s and 0.025 s, respectively. It is expected that, relative to the ISC 1 cells, the closer proximity of the point of short circuit in the ISC 2 cells resulted in the casing being subject to higher temperatures and pressures, conditions that increase the likelihood of sidewall rupture.

In addition to each of the ISC 2 cells undergoing sidewall rupture, a second hole at the crimp fold appeared to form in line with the ISC device (label B in Fig. 8b). The formation of the hole at the crimp was not captured *via* radiographs, but it is expected that the crimp fold acted as a baffle to the escaping fluidized material. It can be inferred that the heating rate of the steel casing due to the flow of broken down material exceeded the rate of heat dissipation at the crimp fold, leading to a temperature increase to above the melting point of the steel.

3.5. Role of the central mandrel

The cylindrical mandrel at the centre of the spiral-wound electrode assembly plays an important role in the failure mechanism of commercial cells.[16] Numerous mandrel designs have been developed for a multitude of purposes, such as

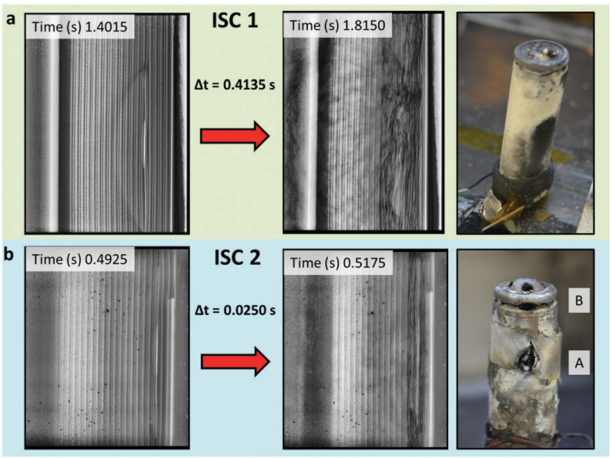

Fig. 8 Radiographs taken at the time of initiation of thermal runaway (left) and the time at which the reaction zone reached the casing (right), along with post-mortem photographs of (a) sample 1 of ISC 1 cells and (b) sample 1 of ISC 2 cells where labels A and B highlight sidewall ruptures. Radiographs of ISC 1 and ISC 2 cells are taken from Movies S1 and S7, respectively (ESI†).

reinforcing cells against crushing and external forces,[44] exerting pressure on the electrode assembly,[45,46] preventing collapse, and maintaining an open channel for gases to reach the vent during failure.[47] The ISC 1 cells contained a 2 g mandrel with a hollow core and an opening on one side in the longitudinal direction (Fig. 9a), whereas the ISC 2 cells did not contain a mandrel.

During thermal runaway, the mandrel in the ISC 1 cells maintained an open channel from the base to the vent through the centre of the cell (Fig. 9a) creating a low resistance path for gases to flow. Even though there was no indication of degradation reactions occurring around the inner regions of the electrode assembly, the intact inner layers of the electrode peeled away from the bulk electrode assembly and flowed towards the vent during the propagation of thermal runaway (indicated by the yellow arrow at 2.0020 s in Fig. 9a). At the same time the mandrel wobbled and shifted position, indicating that the flow rate of gases through and around the mandrel caused enough shear stress for the electrode layers to peel away from the bulk assembly.

As seen in previous work,[16] without an internal mandrel the electrode assembly can collapse, blocking the flow of gas, and increasing the risk of the cell reaching its burst pressure. By preventing internal collapse of the electrode assembly and providing a clear path through which gases can flow during thermal runaway, it is expected that the central mandrel helps

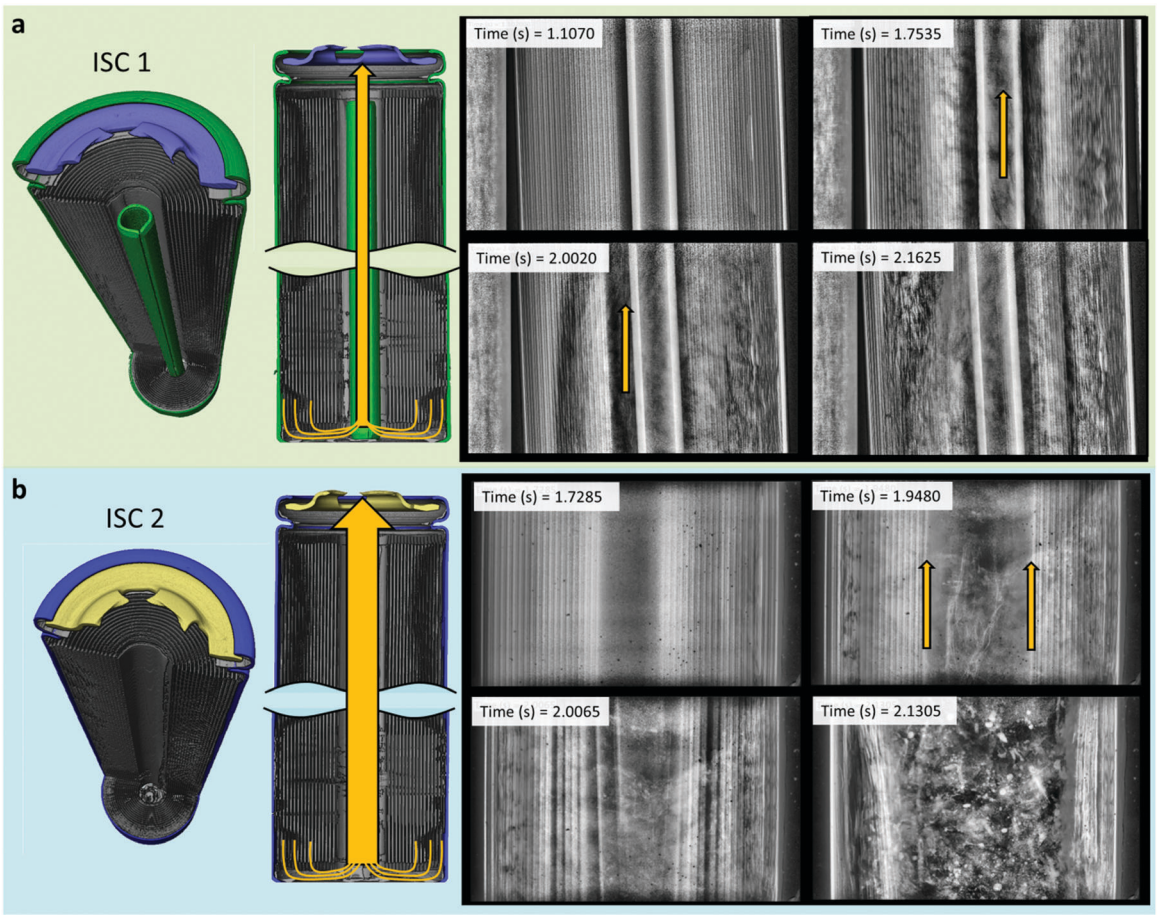

Fig. 9 3D illustrations and time-stamped radiographs of (a) the ISC 1 cells (radiographs from sample 3, Movie S3, ESI†) and (b) the ISC 2 cells (radiographs from sample 2, Movie S8, ESI†), showing the expected path of gas flow through the core of the cell, and an opening forming around the mandrel due to inner spiral-wound layers peeling away and ejecting.

reduce this risk, along with the risk of sidewall rupture. However, the electrode assembly did not collapse in the ISC 2 cells, which may be due to the core of the assembly being tightly packed with excess separator. Soon after thermal runaway initiated, the inner layers of the electrode assemblies in the ISC 2 cells started to peel away as gas flowed through the assembly cores. The rate and extent to which the inner layers were peeled away in the ISC 2 cells was much higher than the ISC 1 cells. The peeled layers and direction of ejection are highlighted using yellow arrows in the radiographs of Fig. 9b. By providing a clear path for the gas to flow, the internal mandrel appeared to contribute towards mitigating peeling through reducing the shear stress experienced by the inner assembly layers by the flow of gas. However, due to the limited number of repeat tests, the variability in the results and the vastly different cell designs between ISC 1 and ISC 2, conclusions with high confidence cannot be drawn.

In two of the six ISC 1 cells, the bursting pressure was reached and the contents ejected. In both cases, the mandrel shifted up towards the vent immediately before ejection. The mandrel can then lodge into the cap of the cell as shown in a previous study,[16] where it could provide a clear path for gases to flow from the base of the cell to the vent through the centre of the mandrel; alternatively, the mandrel may partially block the vent and hinder the escape of electrode material. Being the only component within the cell that maintains its rigidity during thermal runaway, the mandrel may also damage the safety devices and components at the crimp of the cell when forced upwards. Ejection of the electrode assembly prevents the reactions from running to completion, hence the rate and quantity of heat generation are inextricably linked to the cell venting mechanism and its propensity to rupture or eject its contents. Peeling caused by the shear stress induced on the inner layers of the electrode assembly of the ISC 2 cells by the flow of gas appeared to fluidize and eject the electrode material before it began to break down exothermically, which may prove beneficial to reducing the overall heat generated during thermal runaway.

3.6. Application of ISC cells for module testing

Through selective placement of the ISC device within 18 650 cells, the most unfavourable failure mechanisms can be consistently induced. For example, by placing the ISC device near the casing of the cell the likelihood of sidewall rupture has been shown to increase.[48] Being able to induce 'worst-case' scenarios on demand is a particularly useful tool for testing the safety of modular systems and the efficacy of safety devices; a module of 18 650 cells may encompass vulnerabilities to specific failure scenarios, *e.g.* sidewall rupture of a specific cell within the module configuration occurring in a specific direction may present the highest risk of cell-to-cell propagation. To explore this scenario, two 2 × 2 modules of 18 650 cells (Fig. 10a) were loaded with an ISC 2 cell oriented such that the ISC device was slightly off-set (towards the centre of the module) from the connecting surface between the ISC cell and cell 2 (Fig. 10b). This orientation presented the highest risk of cell-to-cell propagation by setting the most likely scenario for sidewall rupture to occur in the direction of a neighbouring cell.

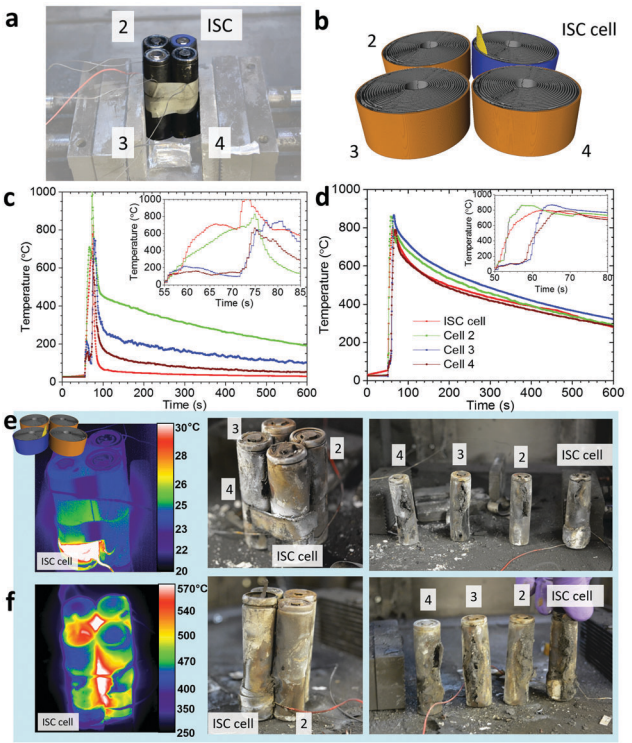

Fig. 10 (a) 2 × 2 module of 18 650 cells with an ISC 2 cell implanted. (b) Reconstructed tomograms of the middle section of the 18 650 cells showing the orientation of the ISC 2 cell (blue). (c and d) Temperature profiles of module 1 and module 2, respectively, with inset temperature profiles showing the moments surrounding the occurrence of thermal runaway. (e and f) Thermal images corresponding to 2 s after heating was applied, and 15 s after thermal runaway of modules 1 and 2, respectively. The inset image shows the placement of the ISC device, and the accompanying post-mortem photographs of the 18 650 cells show the sidewall ruptures on each cell.

In both modules, all four 18 650 cells underwent thermal runaway following the ISC cell, and the temperature profiles in Fig. 10c and d show that the sequence of thermal runaway followed the same pattern; thermal runaway of the ISC cell, followed by cell 2, cell 4, and finally cell 3. The cell closest to the point of initiation of thermal runaway (cell 2) underwent thermal runaway within 2 s of the ISC cell, due to the heat from the short circuit and thermal runaway being concentrated at the side of the ISC cell that made contact. After *ca.* 15 s, cells 3 and 4 underwent thermal runaway, where both cells are expected to have experienced similar heat from the ISC cell and cell 2. Furthermore, each cell underwent sidewall rupture in the direction of the previously failed cell due to the steel casing being weakened on that side (Fig. 10e and f). The sidewall ruptures in module 2 (Fig. 10f) resulted in the contents of the three neighbouring cells bursting out into the core of the module which caused the slow cooling profile observed in Fig. 10d.

In the case of the 2 × 2 modules tested here, the side from which the risk of propagation of thermal runaway is highest is

shown to be the side which underwent sidewall rupture. This is demonstrated by the drastically different times of thermal runaway in the two neighbouring cells (cell 2 and cell 4), where cell 2, directly in line with the sidewall rupture, experiences runaway much sooner than cell 4. The ISC 2 cell is therefore demonstrated as an effective method for inducing controlled 'worst-case' scenarios within Li-ion battery modules.

4. Conclusions

Until now, inducing internal short circuits similar to those that can occur unpredictably in field scenarios has remained a challenge. The ISC device described here, with a low melting point wax interface between electrodes, provides a means for activating an ISC on-demand and at a pre-determined location within the cell. By knowing the location at which the short circuit occurs, the initiation and propagation of thermal runaway was captured using high-speed radiography. Consistent failure mechanisms were identified; anisotropic rates of propagation (where thermal runaway propagates faster in the longitudinal and azimuthal, compared to the radial, direction by more than an order of magnitude) were shown to lead to cylindrically-shaped fluidized reaction zones. The geometric evolution of the reaction zone resulted in an intact core being encompassed by a fluidized region, reducing the shear stress on the intact electrode assembly and contributing to it shifting towards and clogging the vent. This increased the risk of pressure build-up and cell bursting. An alternative path for pressure release would help avoid the build-up of pressure when the vent is clogged, which could be addressed by including secondary bursting disks that are designed to relieve pressure before the cell ruptures.

The influence of the location of short circuiting and initiation of thermal runaway on the failure mechanism of the cell was explored by placing the ISC device at different radial distances from the casing of the 18 650 cell. Sidewall rupture presents one of the greatest hazards during thermal runaway, and was shown to be more likely when thermal runaway initiates closer to the casing of the cell. The ability to control the location at which thermal runaway nucleates, allows 'worst-case' scenario testing where the short circuit is induced at a pre-determined location that is known to lead to unfavourable outcomes such as sidewall rupture or cell bursting. This may allow manufacturers to test, for example, the minimum thickness of casings or the efficacy of venting mechanisms that are necessary to avoid such occurrences.

The cylindrical mandrel in the core of the electrode assembly was shown to influence the venting process. The mandrel maintains an opening for product gas flow but may also damage the vent and safety devices at the cap of the cell when propelled during thermal runaway. The design of the cylindrical mandrel examined here appeared to reduce the shear stress experienced by the inner layers of the electrode assembly by the flow of escaping gases, which helped mitigate against the inner layers being peeled away. However, it is important to note that due to the limited number of repeat tests presented here, conclusions with high confidence cannot be drawn from these results. Nevertheless, these results do introduce the utility of the ISC device for evaluating safety features in various Li-ion cell designs, and for testing the safety of battery modules and systems in the event of a defective cell short circuiting.

Failure mechanisms such as the cell bursting, sidewall rupture, or contained thermal runaway, each pose different risks. The mechanical design of cells and their tendency to undergo such failures should be considered when assessing their suitability for powering systems. Further studies of the behaviour of specific cell designs under 'worst-case' failure scenarios are needed to achieve a greater understanding of the cell-specific risk. There remains significant scope for assessing the location of shorting that leads to the most unfavourable failure mechanism and thereafter to apply this failure mechanism to modules and battery systems in order to expose vulnerabilities. The combined understanding of individual cell failure as well as the consequences in modular systems would provide valuable insight for model validation as well as the design of safer cells and modules.

Author contributions

D. P. F. conceived, prepared, and carried out the experiments. P. R. S. oversaw the project and provided advice for preparing the experiments. E. D. and M. K. developed and constructed the 18 650 cells with integrated ISC devices. B. T., T. M. M. H, R. J., J. J. B., R. M., and P. R. S. provided assistance during beamtime at the ESRF and DLS. N. T. V., O. V. M., R. A., M. D., M. D. M., and A. R. set up the imaging conditions at their respective synchrotron beamlines and provided advice during the preparation stages. G. H., D. J. L. B., and P. R. S. provided valuable advice to D. P. F. while interpreting results and writing the manuscript.

Acknowledgements

The authors would like to acknowledge funding from the EPSRC (EP/N032888/1, EP/M009394/1), the Royal Academy of Engineering, the STFC (ST/N002385/1) and the National Measurement System. These experiments were performed between beamlines ID19 at the ESRF (Grenoble, France) and I12 at Diamond Light Source (Harwell, UK). Finally, the authors would like to acknowledge the help and support from Rohit Bhagat and Melanie Loveridge from WMG at the University of Warwick.

References

1 B. Nykvist and M. Nilsson, *Nat. Clim. Change*, 2015, **5**, 329–332.
2 T. Tsujikawa, K. Yabuta, M. Arakawa and K. Hayashi, *J. Power Sources*, 2013, **244**, 11–16.
3 S. Yayathi, W. Walker, D. Doughty and H. Ardebili, *J. Power Sources*, 2016, **329**, 197–206.
4 NASA, *Technical Report: NASA Aerospace Flight Battery Program*, NASA Engineering and Safety Centre, 2008.

5 J. Chamary, *Forbes, Why are Samsung's Galaxy Note 7 Phones Exploding?*, 2016.
6 AAIB, Report on the serious incident to Boeing B787-8, ET-AOP London Heathrow Airport on 12 July 2013, 2015.
7 D. P. Abraham, E. P. Roth, R. Kostecki, K. McCarthy, S. MacLaren and D. H. Doughty, *J. Power Sources*, 2006, **161**, 648–657.
8 D. Doughty and P. Roth, *Electrochem. Soc. Interface*, 2012, **21**, 37–44.
9 D. P. Finegan, M. Scheel, J. B. Robinson, B. Tjaden, M. Di Michiel, G. Hinds, D. J. L. Brett and P. R. Shearing, *Phys. Chem. Chem. Phys.*, 2016, **18**, 30912–30919.
10 C.-k. Lin, Y. Piao, Y. Kan, J. Bareño, I. Bloom, Y. Ren, K. Amine and Z. Chen, *ACS Appl. Mater. Interfaces*, 2014, **6**, 12692–12697.
11 P. Röder, N. Baba and H. D. Wiemhöfer, *J. Power Sources*, 2014, **248**, 978–987.
12 M. Gikas and J. Beilinson, *Samsung Investigation Reveals New Details About Note7 Battery Failures*, 2017, consumerreports.org.
13 E. Darcy, *J. Power Sources*, 2007, **174**, 575–578.
14 R. Spotnitz and R. Mullar, *Electrochem. Soc. Interface*, 2012, **21**, 57–60.
15 S. Santhanagopalan, P. Ramadass and J. Zhang, *J. Power Sources*, 2009, **194**, 550–557.
16 D. P. Finegan, M. Scheel, J. B. Robinson, B. Tjaden, I. Hunt, T. J. Mason, J. Millichamp, M. Di Michiel, G. J. Offer, G. Hinds, D. J. L. Brett and P. R. Shearing, *Nat. Commun.*, 2015, **6**, 6924.
17 P. G. Balakrishnan, R. Ramesh and T. Prem Kumar, *J. Power Sources*, 2006, **155**, 401–414.
18 A. Haibel, I. Manke, A. Melzer and J. Banhart, *J. Electrochem. Soc.*, 2010, **157**, A387–A391.
19 P. R. Shearing, N. P. Brandon, J. Gelb, R. Bradley, P. J. Withers, A. J. Marquis, S. Cooper and S. J. Harris, *J. Electrochem. Soc.*, 2012, **159**, A1023–A1027.
20 S. R. Stock, *Int. Mater. Rev.*, 2008, **53**, 129–181.
21 E. Maire and P. Withers, *Int. Mater. Rev.*, 2014, **59**, 1–43.
22 A. Rack, M. Scheel, L. Hardy, C. Curfs, A. Bonnin and H. Reichert, *J. Synchrotron Radiat.*, 2014, **21**, 815–818.
23 M. Ebner, F. Marone, M. Stampanoni and V. Wood, *Science*, 2013, **342**, 716–720.
24 D. P. Finegan, E. Tudisco, M. Scheel, J. B. Robinson, O. O. Taiwo, D. S. Eastwood, P. D. Lee, M. Di Michiel, B. Bay, S. A. Hall, G. Hinds, D. J. L. Brett and P. R. Shearing, *Adv. Sci.*, 2016, **3**, 1500332.
25 H. Maleki and J. N. Howard, *J. Power Sources*, 2009, **191**, 568–574.
26 C. J. Orendorff, E. P. Roth and G. Nagasubramanian, *J. Power Sources*, 2011, **196**, 6554–6558.
27 IEC, *Section 8.3.9 Forced short circuit test*, 2015, ch. 8.3.9.
28 E. Cabrera-Castillo, F. Niedermeier and A. Jossen, *J. Power Sources*, 2016, **324**, 509–520.
29 M. Keyser, E. Darcy, D. Long and A. Pesaran, *US pat.* 9142829B2, 2015.
30 M. Di Michiel, J. M. Merino, D. Fernandez-Carreiras, T. Buslaps, V. Honkimäki, P. Falus, T. Martins and O. Svensson, *Rev. Sci. Instrum.*, 2005, **76**, 043702.
31 M. Shoesmith, D. Long and M. Keyser, *Cylindrical Li-ion Cell Response to Induced Internal Short*, Huntsville, AL, 2013.
32 E. Darcy, M. Keyser and M. Shoesmith, *On-demand Internal Short Circuit Device*, Orlando, FL, 2014.
33 M. Vollmer and K.-P. Mollmann, *Infrared Thermal Imaging: Fundamentals Research and Applications*, Wiley-VCH, 2010.
34 M. Drakopoulos, T. Connolley, C. Reinhard, R. Atwood, O. Magdysyuk, N. Vo, M. Hart, L. Connor, B. Humphreys, G. Howell, S. Davies, T. Hill, G. Wilkin, U. Pedersen, A. Foster, N. De Maio, M. Basham, F. Yuan and K. Wanelik, *J. Synchrotron Radiat.*, 2015, **22**, 828–838.
35 A. Kyrieleis, M. Ibison, V. Titarenko and P. J. Withers, *Nucl. Instrum. Methods Phys. Res., Sect. A*, 2009, **607**, 677–684.
36 M. Basham, J. Filik, M. T. Wharmby, P. C. Y. Chang, B. El Kassaby, M. Gerring, J. Aishima, K. Levik, B. C. A. Pulford, I. Sikharulidze, D. Sneddon, M. Webber, S. S. Dhesi, F. Maccherozzi, O. Svensson, S. Brockhauser, G. Naray and A. W. Ashton, *J. Synchrotron Radiat.*, 2015, **22**, 853–858.
37 V. Titarenko, R. Bradley, C. Martin, P. J. Withers and S. Titarenko, *Regularization methods for inverse problems in X-ray tomography*, 2010.
38 D. D. MacNeil, D. Larcher and J. R. Dahn, *J. Electrochem. Soc.*, 1999, **146**, 3596–3602.
39 V. Deimede and C. Elmasides, *Energy Technol.*, 2015, **3**, 453–468.
40 D. P. Finegan, S. J. Cooper, B. Tjaden, O. O. Taiwo, J. Gelb, G. Hinds, D. J. L. Brett and P. R. Shearing, *J. Power Sources*, 2016, **333**, 184–192.
41 J. Chen, Y. Yan, T. Sun, Y. Qi and X. Li, *J. Electrochem. Soc.*, 2014, **161**, A1241–A1246.
42 G.-H. Kim, A. Pesaran and R. Spotnitz, *J. Power Sources*, 2007, **170**, 476–489.
43 S. J. Harris, A. Timmons and W. J. Pitz, *J. Power Sources*, 2009, **193**, 855–858.
44 J. Kim, S. Woo, J. Kim, Y. Kim, Y. Chang and S. Nam, *US pat.* 7955730B2, 2012.
45 J. K. Kim and S. K. Woo, *US pat.* 7691530B2, 2010.
46 D. K. Kim, *US pat.* 0045052A1, 2014.
47 S. Murashige and A. Naoto, *US pat.* 6811920B2, 2004.
48 E. Darcy, M. Tran and N. Anderson, *18650 Cell Bottom Vent: Preliminary Evaluation into its Merits for Preventing Side Wall Rupture*, Huntsville, AL, 2016.